Pt-functionalized Fe2O3 photoanodes for solar water splitting: the role of hematite nano-organization and the platinum redox state

Michael E. A. Warwick,[‡] Davide Barreca,[†] Elza Bontempi,[§] Giorgio Carraro,[‡] Alberto Gasparotto,*[,‡] Chiara Maccato,[‡] Kimmo Kaunisto,[°,‡] Tero-Petri Ruoko,[°] Helge Lemmetyinen,[°] Cinzia Sada,[#] Yakup Gönüllü,[◊] and Sanjay Mathur[◊]

[‡] *Department of Chemistry, Padova University and INSTM, 35131 Padova, Italy*

[†] *CNR-IENI and INSTM, Department of Chemistry, Padova University, 35131 Padova, Italy*

[§] *Chemistry for Technologies Laboratory, University of Brescia, 25123 Brescia, Italy*

[°] *Department of Chemistry and Bioengineering, Tampere University of Technology, 33101 Tampere, Finland*

[#] *Department of Physics and Astronomy, Padova University, 35131 Padova, Italy*

[◊] *Department of Chemistry, Chair of Inorganic and Materials Chemistry, Cologne University, 50939 Cologne, Germany*

ABSTRACT

Pt/α-Fe$_2$O$_3$ nanocomposites are synthesized on fluorine-doped tin oxide (FTO) substrates by a sequential plasma enhanced-chemical vapor deposition (PE-CVD)/radio frequency (rf) sputtering approach, tailoring Pt content as a function of sputtering time. The chemico-physical properties of the as-prepared systems were extensively investigated by X-ray diffraction (XRD), X-ray photoelectron spectroscopy (XPS), field emission-scanning electron microscopy (FE-SEM), energy dispersive X-ray spectroscopy (EDXS), secondary ion mass spectrometry (SIMS), and UV-Vis absorption spectroscopy, and compared to those of Pt/α-Fe$_2$O$_3$ samples annealed in air prior and/or after sputtering. Results evidenced that the system composition, structure/morphology and optical properties are strongly dependent on processing conditions and could be optimized in view of photoelectrochemical (PEC) applications. To this aim, PEC functional data are also reported and explained based~~basing~~ on transient absorption spectroscopy (TAS) results.

INTRODUCTION

Photoelectrochemical (PEC) water splitting is a promising, environmentally benign method of storing solar energy into hydrogen, an attractive fuel with a high energy density and a clean combustion.[1-3] The key component of a PEC cell is the photoanode, typically consisting of an n-type metal oxide (*e.g.* TiO_2, ZnO, WO_3 or Fe_2O_3) promoting the oxygen evolution reaction (OER) at the semiconductor-liquid junction (SCLJ).[2-6] Among the various anode materials, α-Fe_2O_3 (*hematite*) is considered as a strong candidate because it possesses a suitable band-gap of 2.0-2.2 eV for visible light absorption, it is chemically stable against photocorrosion and can be prepared from cheap, abundant, and non-toxic elements.[1,3,5,7-8] However, *hematite* also presents some drawbacks that detrimentally affect the overall system efficiency, among which the low absorption coefficient ($\alpha^{-1} = 118$ nm at $\lambda = 550$ nm), and poor electrical conductivity coupled with a short hole diffusion length (2-4 nm) are particularly critical.[1,3-4,7,9-10] The consequence of this large discrepancy between photon penetration depth and hole diffusion length is that many charge carriers generated far from the SCLJ recombine before they can reach the semiconductor surface and participate in the desired photochemical reactions.[4]]

To alleviate the above problems and improve the non-optimal optoelectronic properties of *hematite*, recent studies have focused on strategies to decouple photon harvesting and charge carrier exploitation. Within this context, synthesis of nano-organized materials with tailored structure and morphology is commonly employed to shorten the pathway that photoexcited holes (h^+) have to travel to reach SCLJ.[1,3,6-7,9-11]] while improving crystallinity and tailoring crystallographic orientation can enhance charge transport properties.[3] Nonetheless, control of α-Fe_2O_3 nano-organization might also result in a more efficient light harvesting, if a proper tuning in particle size, shape, and defect content is accomplished.[7,12-13] Furthermore, as the

particle size shrinks down also the total surface area exposed to the electrolyte and the density of reaction sites available on the semiconductor surface positively increase.*[2-3,7,11]*

Another successful approach to tune the properties of *hematite* involves its chemical modification by elemental doping or decoration with nanoparticles (NPs) of a different element/compound.*[2-4,8,12]* To this aim, heterocomposites electrodes are a clear example of how creating multiple length scales and material components in a single catalytic system can yield improved performances through the exploitation of various phenomena. For instance, heterojunction formation in composite photocatalysts results in the generation of an internal electric field that extends the lifetime of e^-/h^+ pairs limiting recombination losses, thus facilitating the desired redox reactions.*[2,4,12,14]*] Elemental doping of α-Fe$_2$O$_3$ has been reported to increase its electrical conductivity, enhance its optical absorption coefficient, catalytically improve the surface kinetics of the OER reaction, and also beneficially affect the system morphology and surface area.*[1,3,6,8,10]*

Basing on such premises, we report herein on the plasma enhanced-chemical vapor deposition (PE-CVD) fabrication of α-Fe$_2$O$_3$ nanostructures and their modification by Pt sputtering and eventual annealing in air. Though other researchers previously focused on the preparation of Pt/α-Fe$_2$O$_3$ electrodes for PEC water splitting,*[3,5,8,15-16]* the number of reports available in the literature is limited and further studies are necessary to clarify the exact role of *hematite* nanostructure and morphology, as well as platinum loading and redox chemistry.*[8,12]* In the following, using an extensive multi-technique characterization approach, it will be shown that simple variations in the annealing procedure (*i.e.* performing the annealing step either prior and/or after sputtering) allow to efficiently tailor the composition, structure/morphology and optical properties of the resulting Pt/α-Fe$_2$O$_3$ heterocomposites, yielding to a remarkable

improvement of PEC behavior in hydrogen production via water splitting. In particular, transient absorption spectroscopy (TAS), a powerful tool to monitor the evolution(fate)~~faith~~ of the photogenerated electron-hole pairs, has been used to investigate charge carrier dynamics in *hematite* based photoanodes, showing a clear dependency between charge recombination kinetics and PEC efficiency.*[10,17-20]*

EXPERIMENTAL SECTION

Synthesis. Fe_2O_3 deposits were fabricated by means of a custom-built PE-CVD apparatus equipped with a radio frequency (rf, $\nu = 13.56$ MHz) generator. The diameter of each electrode was 9 cm and the inter-electrode distance was fixed at 6 cm. Growth experiments were performed from Ar/O_2 plasmas for a total duration of 1 hour at 10 W RF-power, operating at 1.0 mbar. The iron precursor $Fe(hfa)_2TMEDA$ (hfa = 1,1,1,5,5,5 - hexafluoro - 2,4 - pentanedionate; TMEDA = *N,N,N',N'* - tetramethylethylenediamine), synthesized according to a previously reported procedure,*[21-22]* was placed in an external vessel heated by an oil bath maintained at 65 °C and transported into the reaction chamber by means of electronic grade Ar (purity = 5.0; flow rate = 60 sccm). The temperature of precursor feeding lines was kept at 140 °C through external heating tapes to prevent detrimental condensation phenomena. Two further auxiliary gas-lines were used to introduce Ar (flow rate = 15 sccm) and electronic grade O_2 (flow rate = 20 sccm) directly into the reactor chamber. Basing on our previous findings,*[13]* Fe_2O_3 growth was performed at 300 °C on FTO-coated glass slides (Aldrich, 735167-1EA, ≈7 Ω/sq; lateral dimensions = 2.0 cm × 1.0 cm; FTO thickness ≈600 nm). Prior to deposition, the substrates were suitably cleaned by iterative dipping in acetone, sulphonic detergent, distilled water, and finally dried under an air flow.

Platinum sputtering on iron oxide samples was carried out in the same reactor used for PE-CVD experiments using electronic grade Ar (purity = 5.0) as plasma source. A platinum target (0.3 mm thick; Alfa Aesar®, 99%) was fixed on the rf electrode, and FTO-supported α-Fe_2O_3 matrices were mounted on a second grounded electrode. Sputtering processes were carried out under the following conditions: substrate temperature = 60 °C; rf-power = 5 W; total pressure = 0.30 mbar; Ar flow rate = 10 sccm. After optimization of the processing parameters, experiment duration was set at 30' or 50' to investigate the influence of Pt loading.

Samples were *ex-situ* annealed in air prior and/or after sputtering at 650 °C, 1 h using a Carbolite HST 12/200 tubular oven.

Characterization. 2D X-ray microdiffraction (XRD^2) measurements were run in reflection mode on a Dymax-RAPID X-ray microdiffractometer, with a cylindrical imaging plate detector, that allows collecting from 0 to 160° (2θ) horizontally and from −45 to +45° (2θ) vertically upon using CuKα radiation. Conventional XRD patterns were then obtained by integration of 2D images.

X-ray photoelectron spectroscopy (XPS) measurements were performed on a Perkin-Elmer Φ 5600ci spectrometer using a standard AlKα radiation (1486.6 eV), at a working pressure lower than 10^{-9} mbar. The reported binding energies (BEs, standard deviation = ± 0.2 eV) were corrected for charging by assigning to the adventitious C1s signal a BE of 284.8 eV.**[23]** The analysis involved Shirley-type background subtraction, and, whenever necessary, spectral deconvolution by non-linear least-squares curve fitting, adopting Gaussian–Lorentzian sum functions. Atomic percentages (at.%) were calculated by peak integration using standard PHI V5.4A sensitivity factors.

Field emission-scanning electron microscopy (FE-SEM) micrographs were performed by a

Zeiss SUPRA 40 VP instrument, operating at an acceleration voltage between 5.0 and 10.0 kV. Line-scan energy dispersive X-ray spectroscopy (EDXS) analyses were carried out by monitoring the FeKα, OKα, and PtMα signals throughout the deposit thickness by an Oxford INCA x-sight X-ray detector (acceleration voltage = 20.0 kV).

Secondary ion mass spectrometry (SIMS) analyses were carried out by means of a IMS 4f mass spectrometer (Cameca) using a 14.5 KeV Cs^+ primary beam (intensity 25 nA, stability 0.2%) and by negative secondary ion detection, adopting an electron gun for charge compensation. The signals were detected in beam blanking mode (*i.e.* interrupting the sputtering process during magnet stabilization periods) in order to improve the in-depth resolution and under high mass resolution configuration to avoid mass interference artefacts. The erosion speed was then evaluated by measuring the depth of the erosion crater at the end of each analysis by a Tencor Alpha Step profilometer with a maximum uncertainty of few nanometers (final value given by the average on 10 measures). The film thickness was determined by analysing the element signal dynamics. The error of the film thickness contains therefore contributions of the element inter-diffusion, of the film roughness and finally of the technique artefacts.

UV-Vis optical absorption spectra were recorded in transmission mode at normal incidence by means of a Cary 50 spectrometer, subtracting the substrate contribution. Optical band-gap energies (E_G) were evaluated by applying the Tauc formula:[21,24-25]

$$(\alpha h\nu)^n = A \ (h\nu - E_G) \ , \tag{1}$$

where hν is the incident photon energy, A is a constant and n is an exponent dependent on the nature of electronic transitions ($n = 2$ for direct transitions).

Photoelectrochemical (PEC) measurements were performed in un-buffered 1 M NaOH solutions (pH = 13.0), using a saturated calomel electrode (SCE) as a reference, a Pt wire as

counter-electrode and the Pt:Fe$_2$O$_3$ nanodeposits as working electrodes. All experiments were carried out under ambient conditions. A copper wire was soldered on the uncovered portion of the FTO substrate to establish an electrical connection, and an epoxy resin was used to seal all the exposed FTO portions, except for the working area of the electrodes.[26] The electrolyte was purged with gaseous nitrogen before each experiment in order to prevent any possible reaction with dissolved oxygen.[8,10,27] Linear sweep voltammetry (10 mV/s) was carried out in a potential range from -1 to 1 V *vs.* SCE using a potentiostat (PAR, Versa state IV), both in the dark and under front side illumination, using a Xe lamp (150 W, Oriel) with an AM 1.5 filter. In general, dark currents (not reported) were two orders of magnitude lower than those obtained under illumination. Potentials with respect to the reversible hydrogen electrode (RHE) scale were calculated using the Nernst equation:[10-11,28-30]

$$E_{RHE} = E_{SCE} + E°_{SCE} + 0.059 \text{ pH}, \tag{2}$$

where E_{SCE} is a measured electrode potential *vs.* the reference electrode used and $E°_{SCE}$ is the reference electrode standard potential *vs.* the normal hydrogen electrode (25 °C).

Transient absorption spectroscopy (TAS) measurements were performed~~conducted~~ on samples having a geometric area of 3×3 cm^2 in a complete PEC cell (PECC-2, Zahner-elektrik). A standard three-electrode configuration was used having a Pt counter-electrode, an Ag/AgCl (3M KCl) reference electrode and a 0.1 M NaOH electrolyte (degassed with N$_2$ prior to experiments). A potential value of 1.6 V *vs.* RHE was selected for the measurements, as it provided~~s~~ an optimal~~um~~ signal-to-noise ratio, by a standard potentiostat (F02A, Faraday MP) to study the charge dynamics at the SCLJ ~~in water splitting~~. Readers are kindly advised to access the supporting information for further experimental details of the TAS measurements in picosecond (ps) and millisecond (ms) timescales.[31] [13]

RESULTS AND DISCUSSION

The Pt/Fe$_2$O$_3$ specimens investigated in the present work were characterized by two different Pt loadings and were analyzed both as-prepared and after various thermal treatments in air, performed either before and/or after Pt sputtering. While annealing prior Pt deposition was expected to influence the morphological and structural features of the oxide matrix,*[13]* post-annealing of Pt/Fe$_2$O$_3$ samples could potentially affect the quality of Pt/Fe$_2$O$_3$ interface, as well as platinum dispersion and oxidation state.[ref] The main preparative conditions for each specimen are summarized in Table 1. For further details the reader can refer to the Experimental Section.

Table 1. Samples labeling as a function of preparative conditions.

Sample name	Pre-annealing	Sputtering time	Post-annealing
Pt(30)	//	30'	//
A+Pt(30)	650 °C	30'	//
Pt(30)+A	//	30'	650 °C
A+Pt(30)+A	650 °C	30'	650 °C
Pt(50)	//	50'	//
A+Pt(50)	650 °C	50'	//
Pt(50)+A	//	50'	650 °C
A+Pt(50)+A	650 °C	50'	650 °C

As a representative example, the top panel in Figure 1 compares the XRD^2 maps of the as-prepared Pt/Fe$_2$O$_3$ sample containing the highest Pt amount (Figure 1(a)) and of the same specimen after a double annealing in air (Figure 1(b)). In both cases, no reflections from Pt-containing species were detected, an effect likely due to the relatively low platinum content and the reduced size of Pt aggregates (see below). Conversely, reflections from the α-Fe$_2$O$_3$ (*hematite*) phase could be clearly appreciated in the XRD^2 images, along with the signals of the underlying FTO substrate.

For a more immediate comparison, the integrated XRD patterns of Pt/Fe$_2$O$_3$ samples both before and after thermal treatment in air are reported in the bottom panel of Figure 1. As can be observed, all diffractograms were qualitatively similar and displayed peaks at 24.0, 33.0, 35.4, 40.6, 49.2 attributable to the (012), (104), (110), (113) and (024) *hematite* reflections.[32] Comparison with the pattern of the powder reference material, also indicated that the present iron oxide samples were preferentially oriented along the [110] direction. This phenomenon is expected to be beneficial for PEC applications as α-Fe$_2$O$_3$ presents improved charge transport properties along this direction.[3,16,33-34] Analysis of peak intensities also revealed that Fe$_2$O$_3$ crystallinity was higher in thermally treated samples than in as-prepared ones, an effect attributed to a decreased grain boundary density, and that is likely favorable for PEC performances.[1]
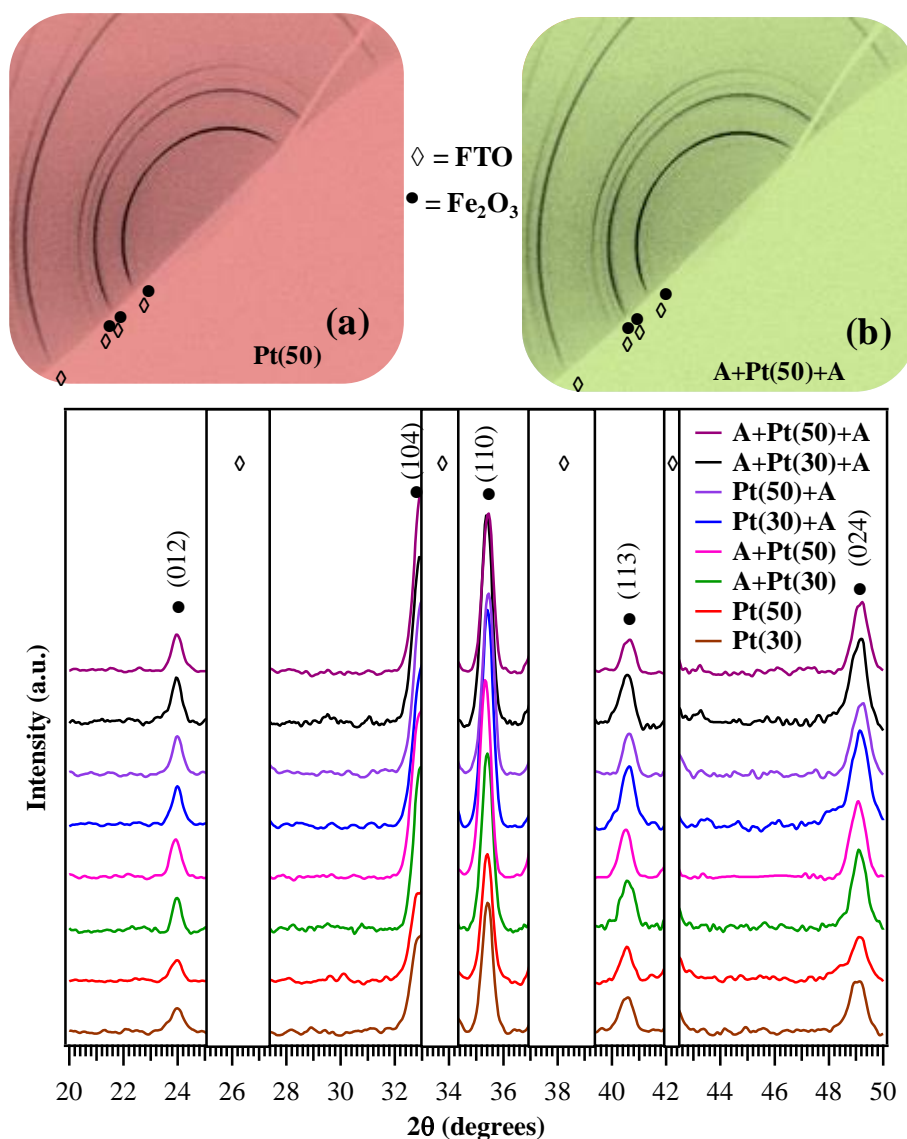
Figure 1. Top: XRD^2 images of two Pt/Fe$_2$O$_3$ samples with the higher Pt loading. (a) shows the as-prepared system and (b) the one annealed twice in air. Bottom: integrated XRD patterns for samples before and after thermal treatment in air. For sake of clarity, FTO peaks are covered and labelled by ◊, while α-Fe$_2$O$_3$ reflections are marked with ●.

XPS surface analyses were subsequently undertaken to investigate the system chemical composition. On all samples, the presence of Pt, Fe and O was detected, along with a minor contribution from adventitious carbon species arising from atmospheric exposure. The spectral features of the Fe2p signal (see Supporting Information, Figure S5(a) and S5(c)) were similar for

11

all specimens and confirmed Fe_2O_3 presence,[5,11,14,35] in line with the above XRD results. Interestingly, XPS data provided insightful information on the Pt chemical state, that exhibited a well evident evolution as a function of processing conditions (Figure S5(b) and S5(d)). As a representative example Figure 2(a) displays the Pt4f signal for the as-prepared sample **Pt(50)**. In this specimen, platinum was mainly present as Pt(II) and Pt(IV) oxides (Pt4$f_{7/2}$ spin-orbit components at 72.6 and 74.6 eV, respectively), while the contribution of Pt(0) (Pt4$f_{7/2}$ at 71.3 eV) was relatively modest.[3,5,12,14] Accordingly, the O1s signal (Figure 2(b)) evidenced not only the presence of *hematite* lattice oxygen (BE = 530.0 eV) and adsorbed water (BE = 533.1 eV) arising from air exposure, but also a major contribution from PtO_x (x = 1,2) at 531.4 eV.[23,36] The above findings suggest that Pt species are appreciably oxidized by interaction with the Fe_2O_3 matrix, an effect likely attributable to the high platinum dispersion within *hematite* (see below).

For comparison, the Pt4f and O1s peaks for the doubly annealed specimen **A+Pt(50)+A** are reported in Figure 2(c) and 2(d), respectively. As can be observed, the main effect of air annealing was to increase the amount of Pt(0) at expenses of Pt(IV) ones. This phenomenon can be traced back to the thermal decomposition of PtO_2 to metallic platinum at temperatures $\geq$ 650°C.[37-38]

A careful deconvolution of the Pt4f peak allowed to determine the relative Pt(0), Pt(II) and Pt(IV) amounts for each synthesized sample. The obtained results are summarized, as a bar plot, in Figure 2(e). The four specimens on the left side of the figure are those that have not been annealed after sputtering. As far as these samples are concerned, platinum is mainly present in its
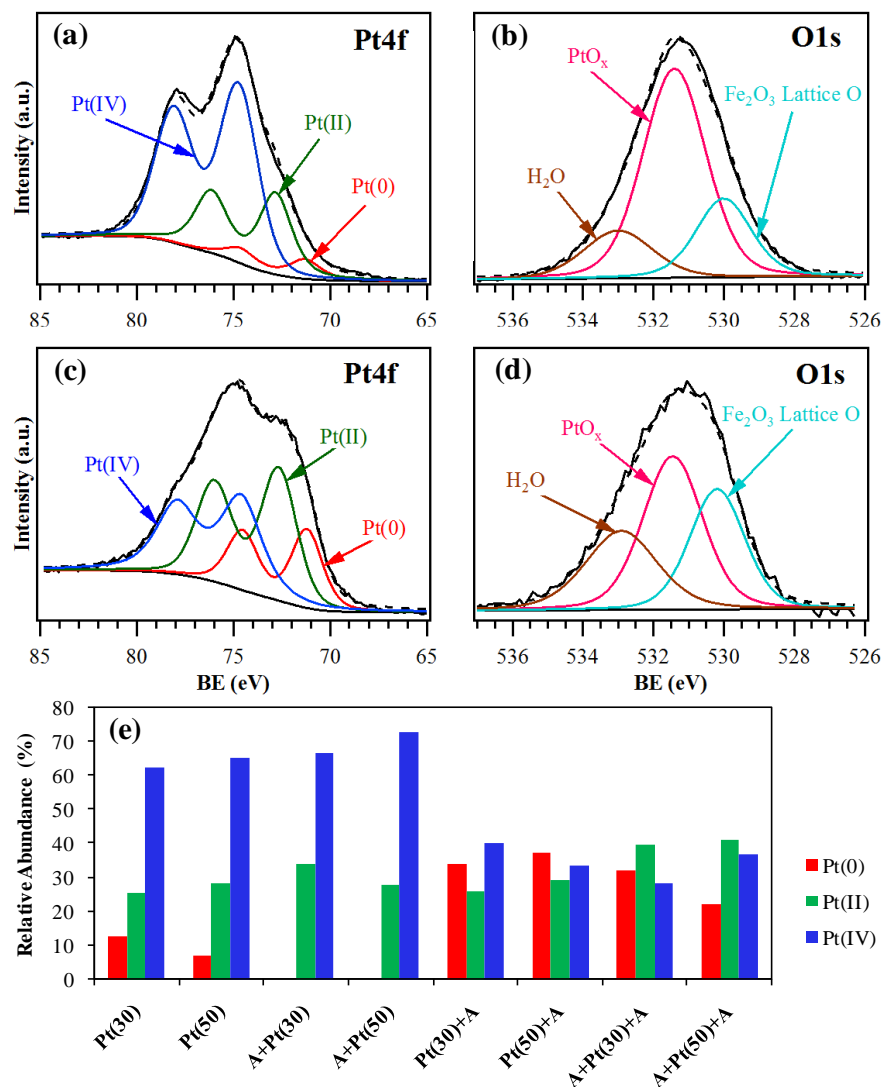
Figure 2. (a) and (b) display the deconvolution of the Pt4f and O1s regions for the as-prepared sample **Pt(50)**. The corresponding figures for the doubly annealed specimen **A+Pt(50)+A** are shown in (c) and (d). (e) bar diagram showing the relative abundance of Pt(0), Pt(II) and Pt(IV) species for the various Pt/Fe$_2$O$_3$ specimens as a function of preparative conditions.

highest oxidation state Pt(IV), while the content of Pt(II) is relatively modest and Pt(0) contribution is even lower. The most evident difference among the above described samples and the four ones on the right side of Figure 2(e) annealed after (and, eventually, also prior) sputtering, is that the latter are characterized by a lower Pt(IV) content and, conversely, by an

13

increased Pt(0) one. Such a result clearly confirms a thermal decomposition of PtO_2 to metallic Pt under the adopted annealing conditions.*[37-38]*

As a final remark on XPS data, it is worth mentioning that annealing also decreased the Pt at.% measured on the sample surface. In principle, such a phenomenon can be due either to an enhanced Pt in-depth dispersion or to a surface redistribution of Pt species. In this regard, a careful analysis of FE-SEM and SIMS results (see below), indicated that the latter phenomenon was likely the dominant one.

Figure 3 shows the plane-view and cross-sectional FE-SEM micrographs of the as-prepared and thermally treated Pt/Fe_2O_3 samples obtained using a sputtering time of 50'. Prior annealing, the surface morphology of **Pt(50)** (Figure 3(a)) resembled the one of bare iron oxide,*[13]* an effect ascribable to the use of mild sputtering conditions and to the low platinum loading. As a matter of fact, the iron oxide deposit was formed by dendritic structures (length = XX nm; lateral size = YY nm) grown perpendicular to the substrate [??? and preferentially oriented along the [110] direction, (see XRD results)????], and whose surface appeared uniformly decorated by Pt particles of 4 ± 1 nm. Figure 3(b) displays the morphology of sample **Pt(50)+A**, obtained by platinum sputtering on α-Fe_2O_3 and subsequent air annealing. As can be observed, the morphology of the *hematite* matrix, though more rounded especially close to the substrate, was still reminiscent of the pristine one (compare Figure 3(b) with 3(a)), and only a modest size increase of Pt NPs (7 ± 2 nm) took place on the sample surface.

In a different way, when annealing was performed prior sputtering (sample **A+Pt(50)**), *hematite* underwent a severe morphological rearrangement, its texture becoming much more rounded and featureless than the corresponding as-prepared material (compare Figure 3(c) with 3(a)). A similar topology was detected also on specimen **A+Pt(50)+A** (Figure 3(d)), that is

formally obtained from the previous sample after a second hour of annealing. To this aim, basing on a statistical analysis of FE-SEM data, the main difference among the two samples is a slight dimensional increase of Pt NPs from 6 ± 2 nm to 8 ± 2 nm.
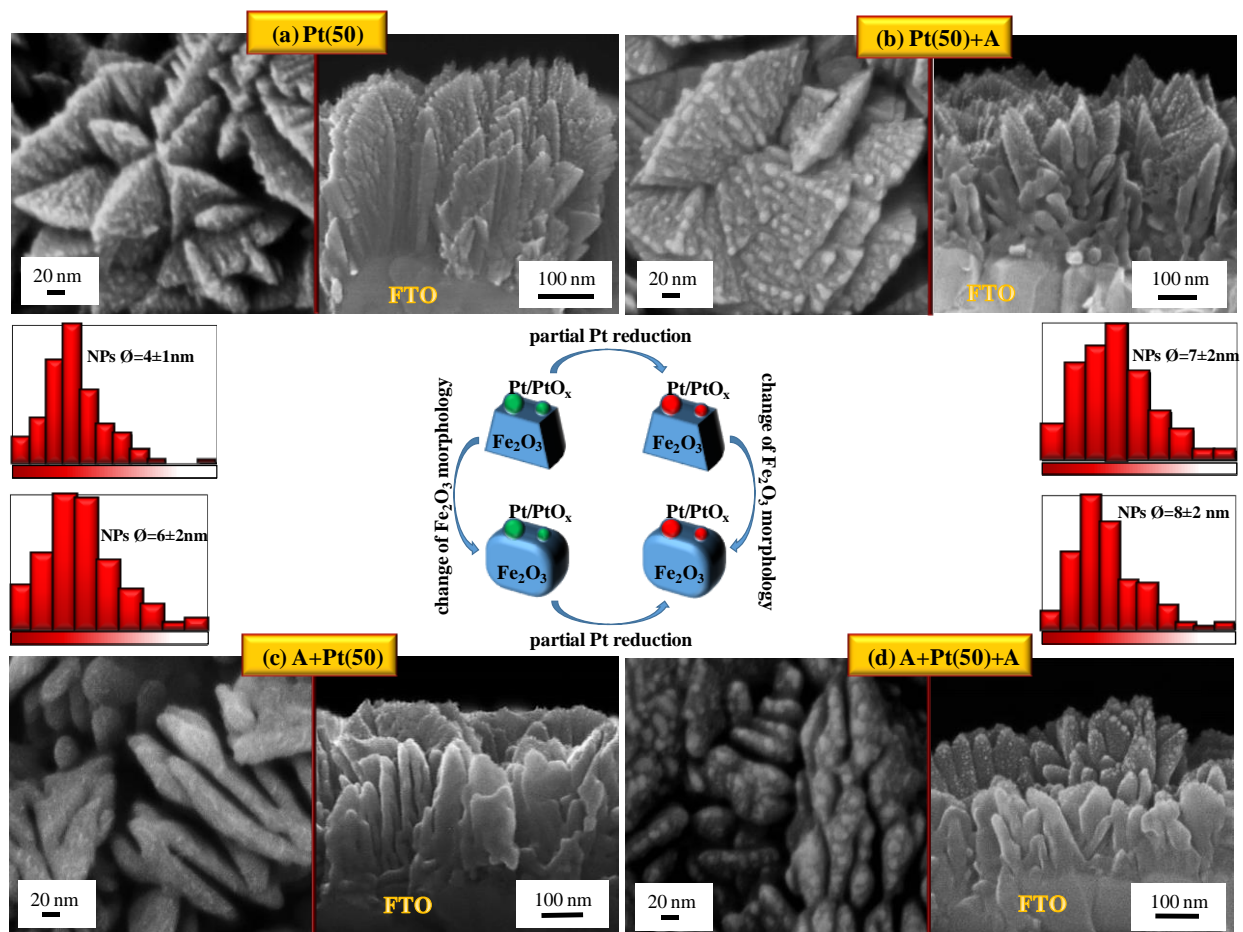
Figure 3. Plane-view (left) and cross-sectional (right) FE-SEM images of as-prepared and annealed Pt-containing Fe_2O_3 samples obtained with a sputtering time of 50'. Close to each specimen, the histogram of Pt particle size is also reported. The sketch at the center of the figure graphically displays the main morphological and chemical differences among the four samples.

As a whole, basing on XPS and FE-SEM results, the above data can be explained taking into account two main thermally activated phenomena: i) when annealing is performed after Pt sputtering (compare Figure 3(b) with 3(a) and 3(d) with 3(c)), the supply of thermal energy

15

results in the thermal decomposition of PtO_2 to Pt, and the morphology of Fe_2O_3 is almost preserved; ii) when annealing is performed prior sputtering (compare Figure 3(c) with 3(a) and 3(d) with 3(b)) it can not affect the Pt redox state (Pt being absent) but, modifies the morphological organization of *hematite* activating diffusion and coalescence processes [???leading to an improved crystallinity and higher porosity???]. The above phenomena, detected also on samples prepared using a sputtering time of 30' (Figure S1), are sketched in a pictorial way, in the central panel of Figure 3.

SIMS in-depth analysis (Figure 4) indicated that, irrespective of the sputtering time and annealing conditions, Fe distribution was homogenous throughout the deposit and resulted in a sharp and well defined interface with the substrate. As far as Pt is concerned, its signal decayed into the *hematite* layer with an erfc profile, as typically observed fort thermal diffusion processes.[14] In all samples, Pt presence (calculated at 16% of the Pt signal maximum) extended up to a depth of 105 ± 10 nm, indicating a high Pt dispersion within the oxide matrix. Such an effect can be traced back to the adopted synthetic strategy, taking advantage on the infiltration power of the sputtering technique and the high porosity of the PE-CVD matrix.[14,39] Nonetheless, despite the above similarities, samples fabricated using a sputtering time of 50' were characterized by an higher Pt content. This effect can be appreciated from the initial value of the Pt ionic yield (compare Figure 4(a)-(b) with Figure 4(c)-(d)) and was confirmed in a more quantitative way by the ratio between integrals of Pt signals in different specimens. In particular, such a calculation indicated that the Pt amount in samples synthesized using a sputtering time of 50' was nearly two times higher than in the case of 30'. This result is in agreement with EDXS data (not reported) that revealed a Pt weight percentage of ca. 3 and 5 wt.% for sputtering times of 30' and 50', respectively. It is finally worthwhile observing that,

though annealing did not enhance Pt dispersion within *hematite*, it promoted an appreciable Sn out-diffusion from the FTO substrate into the *hematite* layer (Figure 4). Such an effect might positively impact on light harvesting and charge transport phenomena, and hence result in improved PEC performances.*[3,7]*
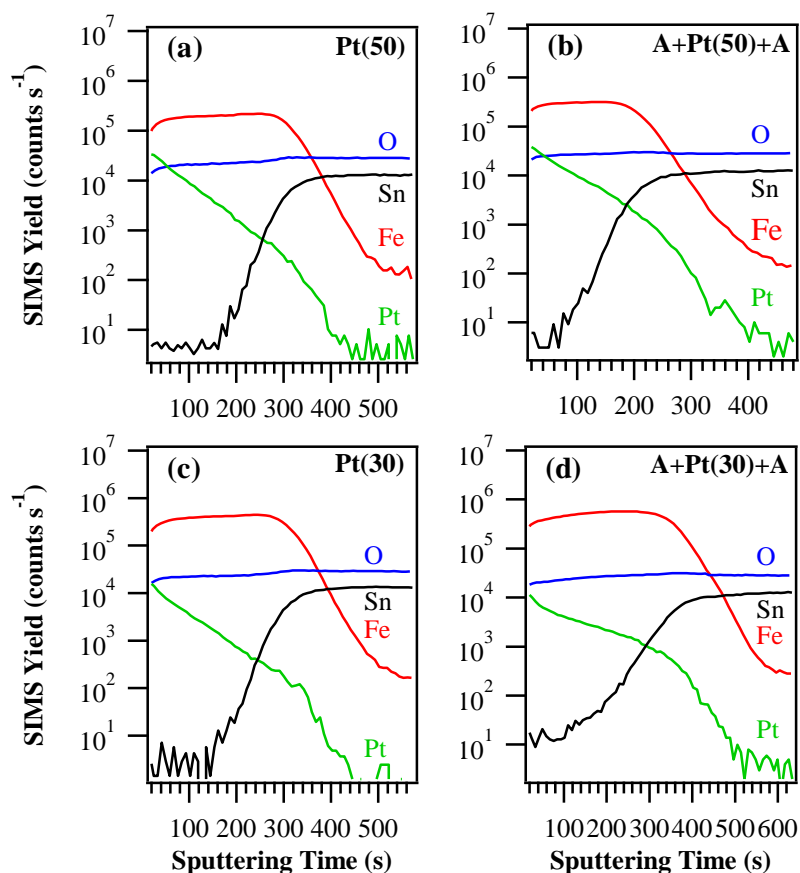
Figure 4. SIMS profiles for the as-prepared and doubly air annealed samples synthesized using a sputtering time of 50' (a, b) and 30' (c, d).

Pt/Fe$_2$O$_3$ samples were finally analyzed by UV-Vis spectroscopy. Basing on experimentally measured absorption spectra and FE-SEM cross-sectional data (average deposit thickness = 365 ± 30 nm), the absorption profiles given in Figure 5 were obtained for samples containing the highest Pt loading (50'). Similar data were gained for a sputtering time of 30' (not reported).
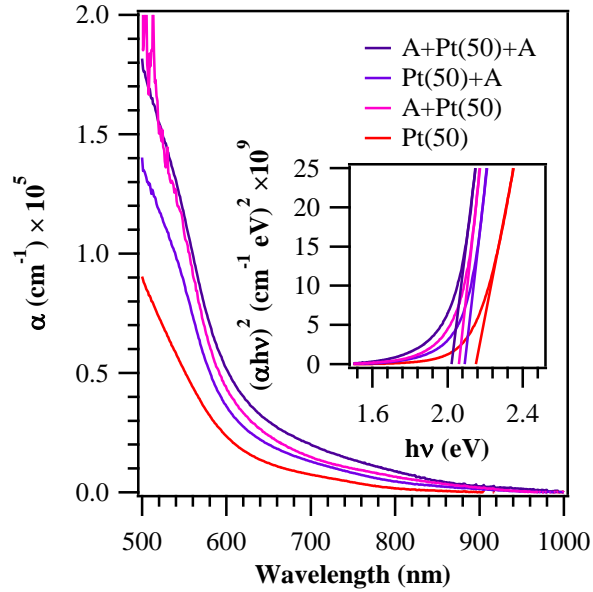
Figure 5. Absorption coefficient as a function of wavelength for Pt/α-Fe$_2$O$_3$ samples synthesized using a sputtering time of 50'. The insets show the corresponding Tauc plots.

As a general rule, the trends of absorption coefficient *vs.* wavelength strongly resembled those of Pt-free systems,[13] indicating that, irrespective of the sputtering time, Pt species did not appreciably contribute to light harvesting. As a consequence, any eventual difference among Pt-containing samples has to be related to the effect of air annealing on the iron oxide matrix. To this aim, all specimens displayed the typical profile of *hematite* films with a sub-band-gap scattering tail in the 600-750 nm region whose intensity increased for thermally treated samples.[7] Consistently with *hematite* band-gap, a sharp increase of the absorption coefficient occurred between 500 and 600 nm, where a shoulder was also detected for annealed systems. Such a phenomenon, resulting in a concomitant decrease of light penetration depth values (α^{-1} at λ = 550 nm) from 196 nm (**Pt50**) to 86 nm (**A+Pt50+A**), can be traced back to a parallel enhancement of the system crystallinity, and is one of the key factors influencing PEC properties.[3,7,13,40] Similarly to previous works,[7] the beneficial effect of air annealing on

18

light absorption properties was also confirmed by the Tauc plots reported as insets in Figure 5, evidencing a slight decrease (ca. 0.1 eV) of band-gap values for all thermally treated samples.

PEC performances of the target materials were evaluated by measuring the current-voltage characteristics. As is well known, the photocurrent observed under illumination is a direct measure of the water splitting rate, reflecting the number of charge carriers produced from the incident light and their subsequent participation in water oxidation at the photoanode and hydrogen reduction at the counter-electrode.[5,8] Photocurrent values at 1.23 V *vs*. RHE are summarized for all specimens in Figure 6, that also provides a sketch for the main phenomena responsible for the detected trends.

As a matter of fact, photocurrent values for as-prepared **Pt(30)** and **Pt(50)** specimens were higher than those pertaining to bare Fe_2O_3 synthesized under the same PE-CVD conditions reported herein,[13] and slightly increased with platinum sputtering time, *i.e.* overall Pt loading in the resulting nanocomposites. This enhancement indicates that Pt dispersion results in a higher *hematite* activity in the oxygen evolution reaction,[5,27] an effect traced back to an increase of Fe_2O_3 electrical conductivity [1,3,5,7-8,15]] and retarded intrinsic charge carrier recombination as a consequence of Pt doping. As a general trend, thermal treatments performed both prior and after Pt functionalization produced an increase of the photocurrent values. This phenomenon can be traced back to a concurrence of different causes [1,8,10,15,27]. Basing on the above discussed data, air annealing promoted a systematic enhancement of XRD peak intensities (Figure 1), indicating the formation of more crystalline materials [27], with a lower content of trapping defects for photogenerated charge carriers [1,15]. In addition, annealing also resulted in an improved light absorption, as testified by Figure 5. Finally (see above and Figure 4), thermal treatments also promoted tin diffusion from the FTO substrate into *hematite*, a phenomenon

likely resulting in a higher electrical conductivity *[33,41-42]* and enhanced interfacial reaction kinetics of photogenerated holes,*[6]* ultimately producing higher photocurrents.*[30]*
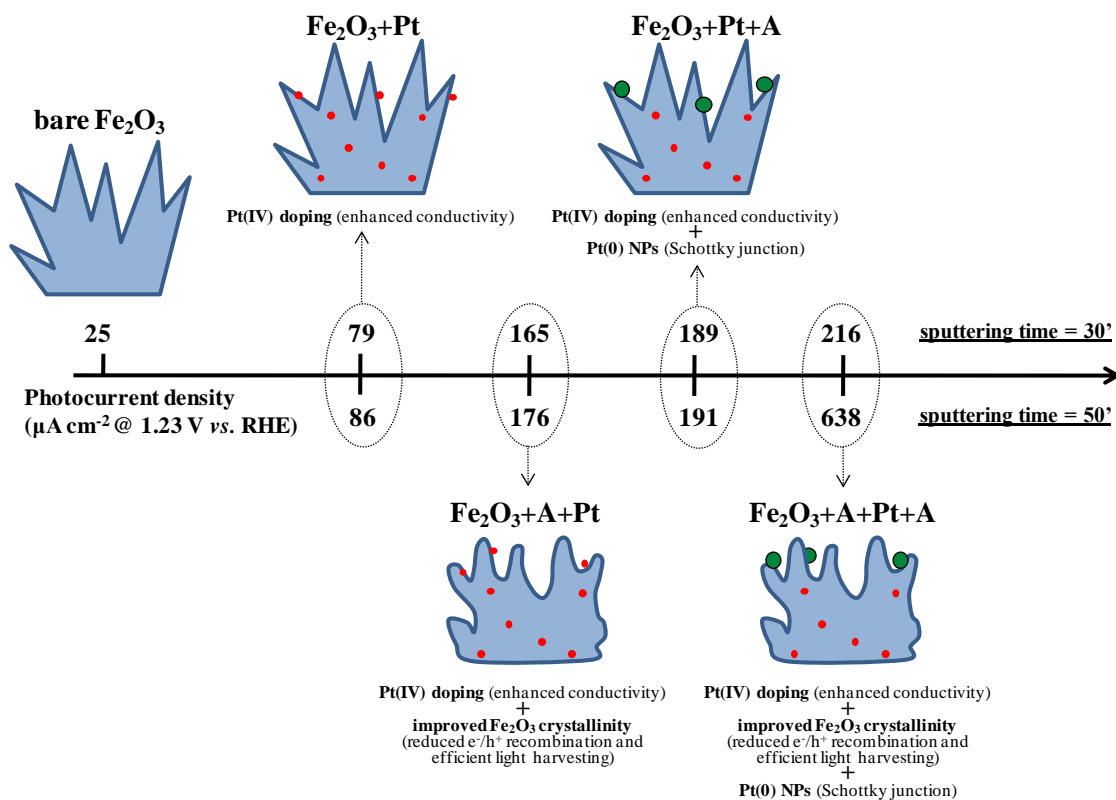
Figure 6. Photocurrent values at 1.23 V *vs*. RHE (the theoretical water oxidation potential) for the synthesized Pt/Fe$_2$O$_3$ samples, along with the corresponding bare Fe$_2$O$_3$ specimen.*[13]*

More specifically, when annealing is performed on Fe$_2$O$_3$ systems *before* platinum deposition (samples **A+Pt(30)** and **A+Pt(50)**), the main resulting variations concern the morphological organization of iron(III) oxide systems. As displayed in Figures 3(c) and S1(c), the structures appear more rounded and partially fused together, confirming a lowered grain boundary content,*[13]* and, in turn, a suppressed recombination of photogenerated electrons and holes,*[16,43]* which is beneficial for PEC performances.*[1]* On the other hand, if thermal treatments are carried out *after* Pt sputtering over Fe$_2$O$_3$ systems (samples **Pt(30)+A** and **Pt(50)+A**), photocurrents are further increased compared to the corresponding as-prepared

heterocomposites (compare Figure 6). In this case, Figures 3(b) and S1(b) indicate that Fe_2O_3

morphology more closely resembles that of samples prior annealing. As a consequence, the main

effect responsible for the improved PEC performances should be related to the variation in the

platinum redox state. In fact, XPS data (see Figure 2) clearly indicated that post-annealing results

in the thermal decomposition of PtO_2 to Pt(0) species, whose presence likely promotes a

beneficial electronic coupling between the metal and the semiconductor,[44] favoring a better

separation of photo-produced electrons and holes. In an attempt to carry out a complete reduction

of Pt-containing species to metallic platinum, hydrogen plasma treatments were carried out and

the results are discussed in detail in the Supporting Information section.

Regarding samples subjected to annealing both *before* and *after* platinum deposition

(**A+Pt(30)+A**, **A+Pt(50)+A**), their functional performances synergistically benefit from all the

above described phenomena, and, in fact, they presented the best PEC behavior in the whole

series (Figure 6). To better appreciate this effect, Figure 7 reports the photocurrent density *vs.*

applied potential curves for Pt/α-Fe_2O_3 nanosystems characterized by the higher (a) and the

lower (b) Pt loading, comparing the photoresponses of as-prepared samples (**Pt(30)**, **Pt(50)**)

against those of the doubly annealed ones (**A+Pt(30)+A**, **A+Pt(50)+A**). As can be observed,

irrespective of Pt deposition time, the photocurrent values at 1.23 V *vs.* RHE underwent an

appreciable increase after thermal treatment. In addition, photocurrent onset shifted to negative

potential by > 0.5 V after the double annealing, improving the j values at lower bias voltages,

similarly to the case of other Au and Pt/Fe_2O_3 nanocomposite systems.[5,44] This beneficial

phenomenon, confirming an enhanced charge transfer,[5] reflected the activity of Pt(0) species

[8,12,27,45], speeding up the reaction kinetics and reducing carrier recombination.[4,10,46]

In particular, the significant photocurrent increase occurring for sample **A+Pt(50)+A** with

respect to the **Pt(50)** one (Figure 7(a)) throughout the potential range $0.8 - 1.7$ V *vs*. RHE revealed that a much larger number of photocarriers participated to water splitting.[5] In this case, the absence of any specific saturation *plateau* at more positive potentials indicates an efficient charge separation upon illumination,[10] confirming that PEC performances improved with Pt content in the target Pt/α-Fe_2O_3 specimens.
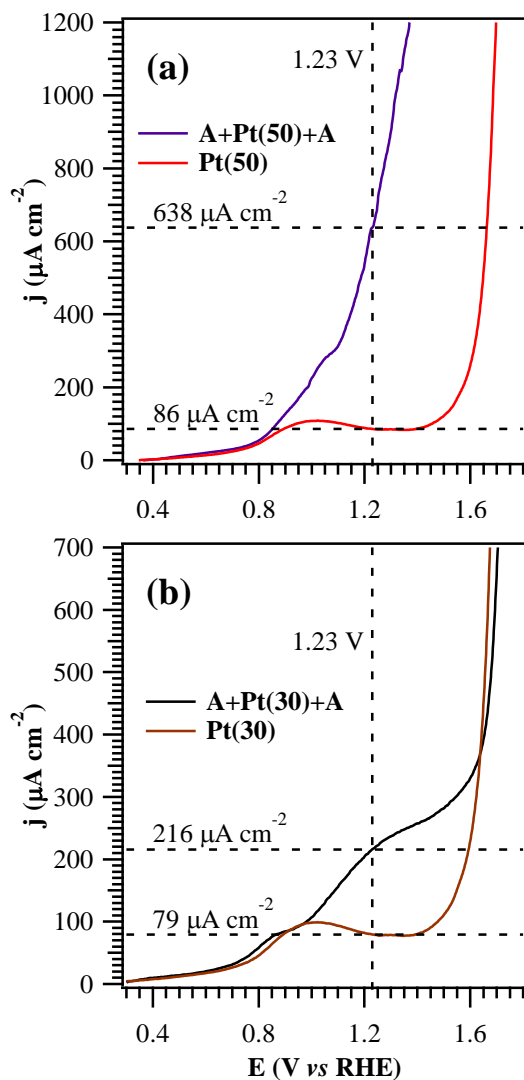

Figure 7. Photocurrent density *vs*. applied potential curves for selected Pt/α-Fe_2O_3 specimens obtained with a sputtering time of 50' (a) and 30' (b). Sample labeling as in **Table 1**.

The increase of photoelectrochemical performances with Pt content is also likely determined

by the concomitant lowering of the charge transfer resistance,[1] increasing the system conductivity,[15] and reduction in the Debye length. The latter phenomenon shrinks the space-charge layer width and, consequently, strengthens the electric field across the space charge layer.[5,8] Consequently, the transit time through the depletion layer is decreased, enhancing, in turn, the separation and transport of photogenerated charge carriers.[12,27] Remarkably, the photoefficiency of the **A+Pt(50)+A** specimen (j ≈ 1200 µA cm^{-2} at 1.40 V) was higher than that reported for bare Fe_2O_3 photoelectrodes,[7,28,41,47-55] and also compared favorably not only with *hematite* films variously doped [6,26,30,56-59] or functionalized,[28-29,44,60-63] but also with previous Pt-containing Fe_2O_3 systems.[8,10,16,27] Thus, the present Pt/α-Fe_2O_3 nanosystems stand as promising candidates for practical utilization in PEC cells.

In order to gain a deeper insight into the ~~above discussed~~ PEC performances and ~~to investigate~~ the photogenerated charge carrier dynamics, TAS analyses were undertaken on two selected specimens, namely **Pt(50)** and **A+Pt(50)+A**. These specimens were chosen as representative taking into account that they present the highest photocurrent variation, and, in the case of sample **A+Pt(50)+A**, the best photoresponses ~~was~~ recorded. Dynamics of photogenerated charge carriers, following the band-gap photoexcitation at 355 nm, were examined by using ps and ms transient absorption spectroscopies. The TAS experiments in a ps time resolution were performed~~carried out~~ to investigate intrinsic charge carrier recombination characteristics, following the excitation laser pulse. A probe wavelength of 650 nm was selected for data elaboration as it represents the value at which the maximum photohole amplitude is ~~typically~~ observed in hematite.[18] Figure 8 displays normalized absorption decay profiles of the as-prepared and doubly annealed Pt/α-Fe_2O_3 specimens in a 0-100 ps timescale. Four-exponential fittings were required to obtain reasonable fit quality, demonstrating the ~~a~~ complex decay nature

of ~~the~~ photoinduced charges in the *hematite* photoanodes in the ultra-fast time range. ~~By fitting,~~ time constants (τ) of 0.1, 1.9, 60, and 5500 ps and 0.4, 5.6, 115, and 7500 ps were obtained for **Pt(50)** and **A+Pt(50)+A**, respectively, showing the intrinsically rapid electron-hole recombination. The sample subjected to ~~the~~ thermal treatment experienced a decreased charge carrier recombination rate providing an enhanced photohole lifetime, as illustrated in~~revealed by~~ Figure 8. This shows the key role of the *ex-situ* thermal treatment of Pt/α-Fe$_2$O$_3$ to prolong the carrier lifetime~~, finally~~ leading to enhanced photocatalytic performances.
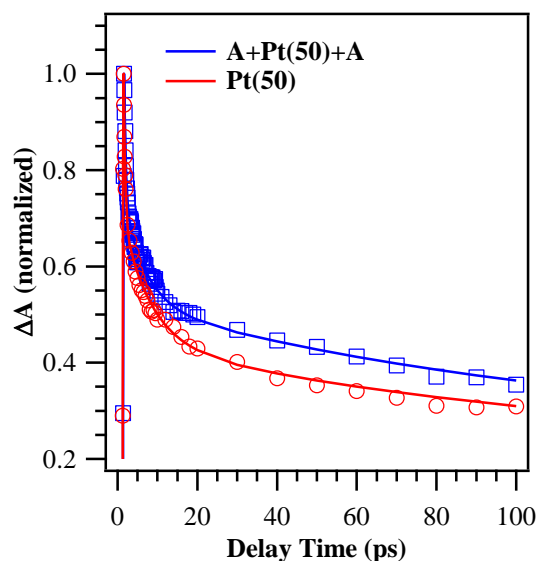
Figure 8. Normalized ultrafast transient absorption decays of Pt/α-Fe$_2$O$_3$ ~~specimens~~ measured at a probe~~ing~~ wavelength of 650 nm. The solid lines represent exponential fits of the raw data.

Transient absorption traces for the Pt/α-Fe$_2$O$_3$ specimens in a ms timescale before and after thermal treatment in air are shown in Figure S6 (see Supporting Information). The annealing enhanced~~s~~ charge carrier lifetime also in a ms timescale, as confirmed by the recombination time constants obtained by bi-exponential fitting (5 *vs.* 22 ms and 140 *vs.* 4200 ms for samples **Pt(50)** and **A+Pt(50)+A**, respectively) of the decay profiles. Thus, the lifetime of the photoholes is extended to a second time range upon annealing of Pt/α-Fe$_2$O$_3$, a key necessity for efficient water

oxidation [vaikka Cowan_JACS_2011]. The prolonged lifetime both in the ps and ms timescale is attributed to enhanced film crystallinity, reducing number of recombination sites in the *hematite*-based nanodeposits upon thermal treatment, being beneficial for the photocatalytic water splitting efficiency.*[18-19]*

CONCLUSIONS

In summary, $Pt/\alpha-Fe_2O_3$ nanosystems have been prepared by means of an original rf-sputtering + PE-CVD route, consisting of PE-CVD of Fe_2O_3 nanodeposits on FTO followed by rf-sputtering of platinum and eventual air annealing. In particular, the attention has been devoted to tailoring *hematite* structure/morphology, as well as the Pt content and redox state by a suitable choice of the preparation parameters and *ex-situ* processing conditions.

The obtainment of $\alpha-Fe_2O_3$ nanodeposits with an inherent porosity, along with the infiltration power characterizing rf-sputtering, has enabled to develop high purity $Pt/\alpha-Fe_2O_3$ nanocomposites with a high Pt dispersion into the hosting oxide system. Variations of the sputtering time have allowed to tailor the amount of Pt-containing nanoaggregates, whose dimensions and distribution were directly dependent on thermal treatment conditions. The latter, in turn, governed even the Pt redox chemistry in the target nanomaterials, enabling a precise control over the valence dynamics $Pt(0) \leftrightarrow Pt(II) \leftrightarrow Pt(IV)$ and offering a strategic option to tailor the electronic interplay between the different species. This effect, along with the system morphological variations, directly impacted the system performances in photoelectrochemical water splitting. In this regard, Pt-containing systems showed an enhanced efficiency compared to bare iron(III) oxide photoanodes, consistently with the expected improvement in the electronic and catalytic properties occurring upon functionalization with platinum. In fact, $Pt/\alpha-Fe_2O_3$

photoanodes with the higher metal loading, subjected to suitable treatments, showed an appreciable photoresponse, accompanied by a reduced onset voltage, highlighting their potential for PEC applications. The enhanced water splitting efficiency of the annealed Pt/*hematite* nanodeposits was, at least partly, attributed to the delayed charge carrier recombination, as revealed by TAS analysis in a ps and ms timescale. The prolonged photohole lifetime is attributed mainly to the increased semiconductor crystallinity, enabling the number of ~~more~~ charges ~~time to~~ participating~~e~~ in the oxygen-evolving reaction to increase ~~within their lifetime~~. Overall, the results provided herein pave the way to the engineering of *hematite*-based nanosystems as efficient photoanodes for the conversion of radiant into chemical energy. Nevertheless, to take full advantage of the present heterocomposites, it is of utmost importance to master their nanoscale assembly into targeted three-dimensional structures, possibly characterized by lower nanostructure sizes, closer to the hole diffusion length. Further work in this direction, as well as in the understanding the effect of Pt functionalization on the surface states, mechanism and PEC behavior of *hematite* nanosystems, will undoubtedly be of key importance.

ASSOCIATED CONTENT

Supporting Information. XRD patterns for two composite samples doubly annealed in air and finally H_2 plasma treated, Pt4f and Fe2p XPS signals for all specimens, plane-view and cross-sectional FE-SEM micrographs for Pt/α-Fe$_2$O$_3$ samples synthesized using a sputtering time of 30', as well as atomic force microscopy (AFM) for two representative systems. This material is available free of charge via the Internet at http://pubs.acs.org.

AUTHOR INFORMATION

Corresponding Author

* E-Mail: alberto.gasparotto@unipd.it

ACKNOWLEDGMENTS

REFERENCES

[1] J.Y. Kim, G. Magesh, D.H. Youn, J.-W. Jang, J. Kubota, K. Domen, J.S. Lee, Scientific Reports 3(2013) 2681.

[2] L. Li, P.A. Salvador, G.S. Rohrer, Nanoscale 6(2014) 24-42.

[3] Y. Ling, G. Wang, D.A. Wheeler, J.Z. Zhang, Y. Li, Nano Letters 11(2011) 2119-2125.

[4] S. Linic, P. Christopher, D.B. Ingram, Nat Mater 10(2011) 911-921.

[5] A. Mao, N.-G. Park, G.Y. Han, J.H. Park, Nanotechnology 22(2011) 175703.

[6] H.K. Dunn, J.M. Feckl, A. Muller, D. Fattakhova-Rohlfing, S.G. Morehead, J. Roos, L.M.P. Peter, C. Scheu, T. Bein, Physical Chemistry Chemical Physics 16(2014) 24610-24620.

[7] K. Sivula, R. Zaboril, F.L. Formal, R. Robert, A. Weidenkaff, J. Tucek, J. Frydrych, M. Grätzel, Journal of the American Chemical Socierty 132(2010) 7436-7444.

[8] Y.-S. Hu, A. Kleiman-Shwarsctein, A.J. Forman, D. Haxen, J.-N. Park, E.W. McFarland, Chemistry of Materials 20(2008) 3803-3805.

[9] T.J. LaTempa, X. Feng, M. Paulose, C.A. Grimes, The Journal of Physical Chemistry C 113(2009) 16293-16298.

[10] S. Shen, M. Li, L. Guo, J. Jiang, S.S. Mao, Journal of Colloid and Interface Science 427(2014) 20-24.

[11] A. Mettenbörger, T. Singh, A.P. Singh, T.T. Järvi, M. Moseler, M. Valldor, S. Mathur, International Journal of Hydrogen Energy 39(2014) 4828-4835.

[12] H. Liang, X. Jiang, W. Chen, S. Wang, B. Xu, Z. Wang, Ceramics International 40(2014) 5653-5658.

[13] M.E.A. Warwick, K. Kaunisto, D. Barreca, G. Carraro, A. Gasparotto, C. Maccato, E. Bontempi, C. Sada, T.-P. Ruoko, S. Turner, G. Van Tendeloo, Nano Res. xxx(2015) xxx.

[14] G. Carraro, D. Barreca, E. Comini, A. Gasparotto, C. Maccato, C. Sada, G. Sberveglieri, CrystEngComm 14(2012) 6469-6476.

[15] H.G. Cha, J. Song, H.S. Kim, W. Shin, K.B. Yoon, Y.S. Kang, Chemical Communications 47(2011) 2441-2443.

[16] Y.-P. Hsu, S.-W. Lee, J.-K. Chang, C.-J. Tseng, K.-R. Lee, C.-H. Wang, International Journal of Electrochemial Science 8(2013) 11615-11623.

[17] F. Le Formal, S.R. Pendlebury, M. Cornuz, S.D. Tilley, M. Grätzel, J.R. Durrant, Journal of the American Chemical Society 136(2014) 2564-2574.

[18] M. Barroso, S.R. Pendlebury, A.J. Cowan, J.R. Durrant, Chemical Science 4(2013) 2724-2734.

[19] S.R. Pendlebury, A.J. Cowan, M. Barroso, K. Sivula, J. Ye, M. Gratzel, D.R. Klug, J. Tang, J.R. Durrant, Energy & Environmental Science 5(2012) 6304-6312.

[20] N.J. Cherepy, D.B. Liston, J.A. Lovejoy, H. Deng, J.Z. Zhang, The Journal of Physical Chemistry B 102(1998) 770-776.

[21] D. Barreca, G. Carraro, A. Devi, E. Fois, A. Gasparotto, R. Seraglia, C. Maccato, C. Sada, G. Tabacchi, E. Tondello, A. Venzo, M. Winter, Dalton Trans. 41(2012) 149-155.

[22] D. Barreca, G. Carraro, A. Gasparotto, C. Maccato, R. Seraglia, G. Tabacchi, Inorganica Chimica Acta 380(2012) 161-166.

[23] J.F. Moulder, W.F. Stickle, P.E. Sobol, K.D. Bomben, Handbook of X-ray Photoelectron Spectroscopy, Perkin Elmer Corperation, Eden Prairie, MN, USA: 1992.

[24] D. Barreca, G. Carraro, A. Gasparotto, C. Maccato, C. Sada, A.P. Singh, S. Mathur, A. Mettenbörger, E. Bontempi, L.E. Depero, International Journal of Hydrogen Energy 38(2013) 14189-14199.

[25] A.P. Singh, A. Mettenbörger, P. Golus, S. Mathur, International Journal of Hydrogen Energy 37(2012) 13983-13988.

[26] S. Kumari, A.P. Singh, Sonal, D. Deva, R. Shrivastav, S. Dass, V.R. Satsangi, International Journal of Hydrogen Energy 35(2010) 3985-3990.

[27] G. Rahman, O.-S. Joo, Materials Chemistry and Physics 140(2013) 316-322.

[28] O. Zandi, J.A. Beardslee, T. Hamann, The Journal of Physical Chemistry C 118(2014) 16494-16503.

[29] L. Steier, I. Herraiz-Cardona, S. Gimenez, F. Fabregat-Santiago, J. Bisquert, S.D. Tilley, M. Grätzel, Advanced Functional Materials (2014) 1-8.

[30] S. Shen, J. Jiang, P. Guo, C.X. Kronawitter, S.S. Mao, L. Guo, Nano Energy 1(2012) 732-741.

[31] D. Sirbu, C. Turta, A.C. Benniston, F. Abou-Chahine, H. Lemmetyinen, N.V. Tkachenko, C. Wood, E. Gibson, RSC Advances 4(2014) 22733-22742.

[32] Pattern N° 33-0664 JCPDS (2000).

[33] N. Mirbagheri, D. Wang, C. Peng, J. Wang, Q. Huang, C. Fan, E.E. Ferapontova, ACS Catalysis 4(2014) 2006-2015.

[34] R. Rajendran, Z. Yaakob, M. Pudukudy, M.S.A. Rahaman, K. Sopian, Journal of Alloys and Compounds 608(2014) 207-212.

[35] G. Carraro, C. Maccato, E. Bontempi, A. Gasparotto, O.I. Lebedev, S. Turner, L.E. Depero, G. Van Tendeloo, D. Barreca, European Journal of Inorganic Chemistry 2013(2013) 5454-5461.

[36] http://srdata.nist.gov/xps.

[37] L.K. Ono, B. Yuan, H. Heinrich, B. Roldan Cuenya, Journal of Physical Chemistry C 114(2010) 22119-22133.

[38] A. Mosquera, D. Horwat, L. Vazquez, A. Gutierrez, A. Erko, A. Anders, J. Andersson, J.L. Endrino, Journal of Materials Research 27(2012) 829-836.

[39] G. Carraro, A. Gasparotto, C. Maccato, E. Bontempi, F. Bilo, D. Peeters, C. Sada, D. Barreca, CrystEngComm 16(2014) 8710-8716.

[40] Y. Qiu, S.-F. Leung, Q. Zhang, B. Hua, Q. Lin, Z. Wei, K.-H. Tsui, Y. Zhang, S. Yang, Z. Fan, Nano Letters 14(2014) 2123-2129.

[41] Y. Ling, G. Wang, D.A. Wheeler, J.Z. Zhang, Y. Li, Nano Lett. 11(2011) 2119-2125.

[42] L. Wang, C.-Y. Lee, P. Schmuki, Electrochim. Acta 91(2013) 307-313.

[43] N.T. Hahn, H. Ye, D.W. Flaherty, A.J. Bard, C.B. Mullins, ACS Nano 4(2010) 1977-1986.

[44] E. Thimsen, F. Le Formal, M. Grätzel, S.C. Warren, Nano Letters 11(2011) 35-43.

[45] M.-H. Pham, C.-T. Dinh, G.-T. Vuong, N.-D. Ta, T.-O. Do, Physical Chemistry Chemical Physics 16(2014) 5937-5941.

[46] P.A. Mangrulkar, V. Polshettiwar, N.K. Labhsetwar, R.S. Varma, S.S. Rayalu, Nanoscale 4(2012) 5202-5209.

[47] A.P. Singh, A. Mettenbörger, P. Golus, S. Mathur, Int. J. Hydrogen Energy 37(2012) 13983-13988.

[48] T.W. Hamann, Dalton Trans. 41(2012) 7830-7834.

[49] Z. Fu, T. Jiang, Z. Liu, D. Wang, L. Wang, T. Xie, Electrochim. Acta 129(2014) 358-363.

[50] J. Liu, M. Shahid, Y.-S. Ko, E. Kim, T.K. Ahn, J.H. Park, Y.-U. Kwon, Phys. Chem. Chem. Phys. 15(2013) 9775-9782.

[51] D. Barreca, G. Carraro, A. Gasparotto, C. Maccato, C. Sada, A.P. Singh, S. Mathur, A. Mettenbörger, E. Bontempi, L.E. Depero, Int. J. Hydrogen Energy 38(2013) 14189-14199.

[52] J. Liu, Y.Y. Cai, Z.F. Tian, G.S. Ruan, Y.X. Ye, C.H. Liang, G.S. Shao, Nano Energy 9(2014) 282-290.

[53] S.C. Riha, B.M. Klahr, E.C. Tyo, S. Seifert, S. Vajda, M.J. Pellin, T.W. Hamann, A.B.F. Martinson, ACS Nano 7(2013) 2396-2405.

[54] R. Rajendran, Z. Yaakob, M. Pudukudy, M.S.A. Rahaman, K. Sopian, J. All. Compd. 608(2014) 207-212.

[55] L. Jia, K. Harbauer, P. Bogdanoff, I. Herrmann-Geppert, A. Ramirez, R. van de Krol, S. Fiechter, Journal of Materials Chemistry A 2(2014) 20196-20202.

[56] I. Cesar, K. Sivula, A. Kay, R. Zboril, M. Grätzel, J. Phys. Chem. C 113(2009) 772-782.

[57] S. Shen, C. Kronawitter, J. Jiang, S. Mao, L. Guo, Nano Res. 5(2012) 327-336.

[58] J. Liu, C. Liang, G. Xu, Z. Tian, G. Shao, L. Zhang, Nano Energy 2(2013) 328-336.

[59] A. Kleiman-Shwarsctein, Y.-S. Hu, A.J. Forman, G.D. Stucky, E.W. McFarland, The Journal of Physical Chemistry C 112(2008) 15900-15907.

[60] L. Steier, I. Herraiz-Cardona, S. Gimenez, F. Fabregat-Santiago, J. Bisquert, S.D. Tilley, M. Grätzel, Adv. Funct. Mater. (2014) DOI: 10.1002/adfm.201402742.

[61] M. Tallarida, C. Das, D. Cibrev, K. Kukli, A. Tamm, M. Ritala, T. Lana-Villarreal, R. Gómez, M. Leskelä, D. Schmeisser, J. Phys. Chem. Lett. (2014) 3582-3587.

[62] L. Fu, H. Yu, C. Zhang, Z. Shao, B. Yi, Electrochim. Acta 136(2014) 363-369.

[63] S. Shen, Journal of Materials Research 29(2014) 29-46.